42nd AIAA Aerospace Sciences Meeting and Exhibit
5 - 8 January 2004, Reno, Nevada

42nd AIAA Aerospace Sciences Meeting and Exhibit
5-8 January 2004 / Reno, NV

TIME-AVERAGE MOLECULAR RAYLEIGH SCATTERING TECHNIQUE FOR MEASUREMENT OF VELOCITY, DENSITY, TEMPERATURE, AND TURBULENCE INTENSITY IN HIGH SPEED NOZZLE FLOWS

Amy F. Mielke*
Richard G. Seasholtz†
NASA Glenn Research Center, Cleveland, OH 44135

Kristie A. Elam‡
Akima Corporation, Fairview Park, OH 44126

Jayanta Panda§
OAI, Brook Park, OH 44142

ABSTRACT

A molecular Rayleigh scattering based flow diagnostic is developed to measure time average velocity, density, temperature, and turbulence intensity in a 25.4-mm diameter nozzle free jet facility. The spectrum of the Rayleigh scattered light is analyzed using a Fabry-Perot interferometer operated in the static imaging mode. The resulting fringe pattern containing spectral information of the scattered light is recorded using a low noise CCD camera. Nonlinear least squares analysis of the fringe pattern using a kinetic theory model of the Rayleigh scattered light provides estimates of density, velocity, temperature, and turbulence intensity of the gas flow. Resulting flow parameter estimates are presented for an axial scan of subsonic flow at Mach 0.95 for comparison with previously acquired pitot tube data, and axial scans of supersonic flow in an underexpanded screeching jet. The issues related to obtaining accurate turbulence intensity measurements using this technique are discussed.

INTRODUCTION

The objective of this work is to obtain high accuracy measurements of time average velocity, density, and temperature in unseeded flows using a nonintrusive, point-wise measurement technique based on molecular Rayleigh scattering. A measure of the flow turbulence intensity is desired as well. The data obtained from these measurements is useful for validation of computational fluid dynamics (CFD) codes. This nonintrusive technique is particularly useful in supersonic flows where seeding the flow with particles is not an option, and where the environment is too harsh for hot wire measurements. A similar Rayleigh scattering technique has been used successfully in the past to make temperature and velocity measurements in harsh environments[1,2]. The presented technique uses a slow scan, low noise CCD camera to record fringes formed by Rayleigh scattered light and reference laser light passing through a Fabry-Perot interferometer. Nonlinear least squares analysis based on a kinetic theory model of Rayleigh scattering is used to obtain density, velocity, and temperature information from the fringe images. A technique for extracting turbulence intensity information from the fringe image data is also investigated. Extracting turbulence intensity information from the fringe image data is a challenge since the fringe is broadened by not only turbulence, but also by thermal fluctuations, aperture effects from collecting light over a range of scattering angles, and laser frequency drift over the integration time of the measurement. The presented technique is used to study subsonic and supersonic air flows in a 25.4-mm diameter nozzle free jet facility.

Point-wise measurements of turbulence intensity are traditionally obtained using hot wire anemometry or Laser-Doppler Velocimetry (LDV)[3,4,5,6]. However, these techniques have obvious disadvantages. Hot wire anemometry requires that a physical probe be placed in the flow field, hence disturbing the true flow characteristics. Although LDV is a nonintrusive technique, it has the disadvantage of requiring seed particles in the flow, which always has difficulties associated with it. Other optical based techniques for measuring turbulence intensity have been investigated. Elliot and Boguszki[7] investigated a filtered Rayleigh scattering technique to make turbulence intensity measurements using a pulsed laser to get instantaneous quantities. Transient gradient spectroscopy (TGS)[8], also known as Laser-Induced Thermal Acoustics (LITA)[9], is a point-wise technique that measures instantaneous temperature, velocity, and species concentrations, and

is capable of providing turbulence intensity information. Bridges et al[10] used Particle Image Velocimetry (PIV) to calculate turbulence in nozzle flows from instantaneous 2-D velocity maps. Nakatani et al[11] developed a pulsed luminescence method in which the turbulence intensity is measured from the diffusion width of the emission according to Taylor's diffusion theory. Garg and Settles[12] developed a technique based on focusing schlieren deflectometry to make turbulence measurements in compressible flows. The presented Rayleigh scattering technique is unique in that it provides simultaneous time-average density, velocity, temperature, and turbulence intensity measurements at a point in a flow field. The ability to make multiple property measurements simultaneously is a valuable tool for jet flow research.

THEORY

Molecular Rayleigh scattering is the result of elastic light scattering from gas molecules. The frequency of the scattered light is equal to the frequency of the incident laser light altered by the Doppler effect due to the motion of the molecules. The Rayleigh scattering spectrum contains information about the gas density, bulk velocity, and temperature. Figure 1 shows a Rayleigh scattering spectrum containing the narrow laser line and the broadened Rayleigh spectral peak. The total intensity of the Rayleigh spectrum is directly proportional to the gas density. The Doppler shift between the laser peak and the Rayleigh peak is proportional to the bulk flow velocity. The width of the Rayleigh spectrum is related to the gas temperature.

For low density gases, the Rayleigh spectrum is accurately modeled by a Gaussian function:

$$S_R(x_f) = \frac{1}{\sqrt{\pi}} e^{-\left(x_f - \frac{\mathbf{K}\cdot\mathbf{u}}{\mathrm{K}a}\right)^2} \tag{1}$$

where x_f is the dimensionless frequency defined as

$$x_f = \frac{2\pi(f - f_0)}{\mathrm{K}a}, \tag{2}$$

a is the most probable molecular speed defined as

$$a = \sqrt{\frac{2\kappa T}{m}}, \tag{3}$$

where κ is the Boltzmann constant, T is the fluid temperature, m is the molecular mass, f-f_0 is the frequency shift between the reference laser light and the Rayleigh scattered light, and **K** is the interaction wave vector that defines the direction of the velocity component, u_k, being measured. As shown in figure 2, the interaction wave vector, and hence the measured velocity component, are defined by the incident and scattered light wave vectors, $\vec{k}_0$ and $\vec{k}_s$, from light incident on a moving particle:

$$\mathbf{K} = \vec{k}_s - \vec{k}_0 \tag{4}$$

$$\mathrm{K} = |\mathbf{K}| = \frac{4\pi}{\lambda}\left[\sin\frac{\chi_s}{2}\right] \tag{5}$$

$$u_k = \mathbf{K}\cdot\mathbf{u}/\mathrm{K} \tag{6}$$

where λ is the wavelength of the incident light, and χ_s is the scattering angle between the incident and scattered light wave vectors. The geometry of the optical arrangement in an experiment can be designed such that the desired velocity component is measured.

For higher density gases, the Gaussian model is not accurate since the Rayleigh spectrum broadens and eventually develops side-lobes as shown in figure 3. A nondimensional parameter y is used to characterize the density regime:

$$y = \frac{p}{\eta \mathrm{K}a} \tag{7}$$

where p is the gas pressure and η is the gas viscosity. Three density regimes are defined for typical 90°-scattering. A low density regime exists for y<<1 where the Gaussian model is valid. A high density regime exists for y>>1 where a Continuum model is valid. The regime for $y \sim 1$ requires the use of a kinetic theory model.[13]

For our application y is approximately 1. A model developed by G. Tenti[14,15] provides a kinetic model of Rayleigh-Brillouin scattering from molecular gases in all density regimes. The TENTI S6 model is the chosen spectrum model for least-squares fitting of our data.

The spectrum of the Rayleigh scattered light is analyzed using a planar mirror Fabry-Perot interferometer operated in the static imaging mode[16]. The fringes at the output of the interferometer are focused onto a CCD detector. The fringe intensity pattern is a function of the Rayleigh spectrum, S_R, and the Fabry-Perot instrument function, I_{FP}. The Fabry-Perot instrument function is:

$$I_{FP}\left[\psi(x_f, r)\right] = \frac{1}{1 + F\sin^2\frac{\psi(x_f, r)}{2}} \tag{8}$$

where $F = \dfrac{1}{\sin^2\left(\dfrac{\pi}{2N_e}\right)}$, (9)

ψ is the phase change of the light between successive reflections given by:

$$\psi = \frac{4\pi\mu d}{\lambda}\left[\frac{\theta_R^2 - \theta^2}{2} + \frac{\lambda a}{c\Lambda}x_f\right], \quad (10)$$

N_e is the effective finesse, μ is the refractive index of the medium in the Fabry-Perot cavity, d is the Fabry-Perot mirror spacing, θ is the angle between the ray and optical axis ($\theta_R = r_R/f_L$, $\theta = r/f_L$), r_R is the fringe radius of the reference laser light, r is the radial position in the image plane, f_L is the fringe forming lens focal length, and $\Lambda = 2\pi/K$.

In our experiment, Rayleigh scattered light from a defined probe volume is collected into a multimode optical fiber. The fiber carries the light to another area where a Fabry-Perot interferometer is used to spectrally resolve the light. A low-noise CCD camera is placed at the output of the Fabry-Perot interferometer and a fringe forming lens focuses the interference fringe pattern onto the CCD detector. The total expected number of photoelectron counts incident on the detector plane without the Fabry-Perot interferometer in the optical path is expressed as:

$$\langle N_R \rangle = \frac{\varepsilon P_0 n L_x \lambda \Omega \Delta t}{h c}\left(\frac{d\sigma}{d\Omega}\right) sin^2 \chi_s \quad (11)$$

where ε is the overall system efficiency including detector quantum efficiency and other losses, P_0 is the power of the incident laser beam, n is the molecular number density, L_x is the probe volume length, Ω is the solid light collection angle, Δt is the data acquisition time, $\left(\frac{d\sigma}{d\Omega}\right)$ is the differential scattering cross-section of the gas molecules, h is Planck's constant, and c is the speed of light. If we assume that illumination is uniform over the entire fiber face, then the model function for the amount of energy collected on the q^{th} pixel of the detector, expressed as photoelectron counts including light at the laser frequency, light scattered from particles (Mie scattering) and background light, as imaged through the Fabry-Perot, is:

$$\langle N_q \rangle = \frac{\langle N_R \rangle}{\pi r_{\max}^2}\int_{y_q}^{y_q+\varepsilon_p}\int_{x_q}^{x_q+\varepsilon_p}\int_{-\infty}^{+\infty} S_R(x_f) I_{FP}(x_f, r)\, dx_f\, dx\, dy + \frac{A_f}{\varepsilon_p^2}\int_{y_q}^{y_q+\varepsilon_p}\int_{x_q}^{x_q+\varepsilon_p} I_{FP}(x_{f_0}, r)\, dx\, dy + \frac{A_p}{\varepsilon_p^2}\int_{y_q}^{y_q+\varepsilon_p}\int_{x_q}^{x_q+\varepsilon_p} I_{FP}(x_f, r)\, dx\, dy + B_g \quad (12)$$

where $r_{\max}$ is the radius of the image of the fiber face, (x,y) are the position coordinates in the image plane, $r = \sqrt{(x-x_0)^2 + (y-y_0)^2}$ where (x_0,y_0) are the coordinates of the center of the fringe pattern, (x_q,y_q) are the coordinates of the lower left corner of the q^{th} pixel, ε_p is the pixel width (square pixels are assumed), A_f is the amount of light at the laser frequency, A_p is the amplitude of the light scattered from particles, and B_g is the amount of broadband light. If the flow is turbulent, the Rayleigh scattering spectrum S_R in equation (12) is replaced by the following spectrum:

$$S_T(x_f, \overline{u_k}, \sigma_{u_k}) = \int_{-\infty}^{\infty} S_R(x_f, u_k)\, p(u_k, \overline{u_k}, \sigma_{u_k})\, du_k \quad (13)$$

and the model of the particle scattering is modified as:

$$\frac{A_p}{\varepsilon_p^2}\int_{y_q}^{y_q+\varepsilon_p}\int_{x_q}^{x_q+\varepsilon_p}\int_{-\infty}^{\infty} p(u_k, \overline{u_k}, \sigma_{u_k}) I_{FP}(x_f, r)\, du_k\, dx\, dy \quad (14)$$

where a Gaussian probability distribution is assumed for the velocity component, u_k,

$$p(u_k, \overline{u_k}, \sigma_{u_k}) = \frac{1}{(2\pi)^{1/2}\sigma_{u_k}} e^{-\frac{1}{2}\left(\frac{u_k - \overline{u_k}}{\sigma_{u_k}}\right)^2}, \quad (15)$$

and the turbulent fluctuations are assumed to be isotropic with standard deviation:

$$\sigma_{u_k} = \left\langle \left(\mathbf{u} - \langle \mathbf{u} \rangle\right)^2 \right\rangle^{1/2} = \left[\left(u_k - \overline{u_k}\right)^2\right]^{1/2} \quad (16)$$

The turbulence intensity is generally defined as:

$$TI = \frac{\sigma_{u_k}}{U_j} \quad (17)$$

where the turbulent fluctuations are normalized by the jet centerline velocity at the nozzle exit, U_j. This model function is used to estimate the unknown parameters from the experimental data.

Measurement uncertainty

The lower bound on the uncertainty in density, velocity, temperature, and turbulence intensity measurements using Rayleigh scattering is set by the photon statistical noise. Estimates of the measurement uncertainty in the unknown parameters for this technique can be obtained by calculating the Cramer-Rao lower bound[17]. For a measurement that is a function of a set of unknown parameters, $\boldsymbol{\alpha} = [\alpha_1, \alpha_2, \alpha_3, ...]$, the variance of the estimates of the parameters α_i is:

$$V(\hat{\alpha}_i) = \left[\Gamma^{-1}\right] \quad (18)$$

where Γ is the Fisher information matrix given (for Poisson statistics) by:

$$\Gamma_{i,j} = \sum_q \frac{1}{\langle N_q \rangle}\frac{\partial \langle N_q \rangle}{\partial \alpha_i}\frac{\partial \langle N_q \rangle}{\partial \alpha_j} \quad (19)$$

A process governed by Poisson statistics is one in which the mean is equal to the variance. In this case, the mean of the photon counts is theoretically equal to the variance of the counts.

The Cramer-Rao lower bound estimates for our actual Fabry-Perot interferometer and CCD system, assuming the TENTI S6 spectrum model for the Rayleigh scattered light and including read noise, overall efficiency of the system, and other significant factors, have been calculated for various flow cases representing a range of *y*-parameter values. The lower bound measurement uncertainty in density, velocity, and temperature when fitting for ρ, u_k, T, σ_{uk}, x_0, and y_0 were about 0.1%, 0.3 m/s, and 0.3%, respectively. Figure 4 shows the lower bound measurement uncertainty in σ_{u_k} for *y*-parameters ranging from 0.75 to 1.9 for σ_{u_k} = 5, 10, and 20 m/s. As *y* increases, the uncertainty level decreases. Also, as σ_{u_k} decreases, the uncertainty becomes even greater to the point where the uncertainty in σ_{u_k} exceeds the actual value of σ_{u_k}.

The ability to extract turbulence information from the spectrum improves as the Rayleigh spectrum deviates from a Gaussian. This occurs only for *y* greater than about 0.8. For *y* less than this value, the Rayleigh spectrum is close to Gaussian and the effect of turbulence broadening, which is assumed to be Gaussian, cannot be separated from the Rayleigh spectrum. The dependence of turbulence measurement on spectral shape indicates that having the right model of the spectrum is extremely important. From the lower bound analysis, we conclude that the ability to obtain meaningful turbulence information is restricted to flows where σ_{u_k} is greater than 10 m/s and *y* is greater than 0.8.

The model of the imaged fringe pattern described above was used to generate simulated images with conditions similar to those expected in our experiment. Simulated images were generated with a known amount of turbulence intensity over a range *TI*=0 to 100% assuming isentropic flow conditions for Mach 0.6. Poisson noise was added to the images. These images were analyzed fitting for ρ, u_k, T, x_0, and y_0, while *TI* was assumed to be 0%. The purpose of this exercise was to determine how the estimated ρ, u_k, and T values vary from the true values if turbulence is ignored. Figure 5 is a plot of the error in temperature as a function of turbulence intensity. This gives an indication of the expected error in the temperature measurement if turbulence is ignored. If the turbulence intensity is less than 40% in this case, the error in the temperature measurement is negligible (less than 2%). The velocity varied by less than 1 m/s and the density varied by less than 2% for turbulence intensities less than 40%. At higher Mach numbers, the error in temperature will be larger for the same turbulence intensity.

EXPERIMENT

Image data were acquired in a free jet and analyzed using the described nonlinear least-squares method to obtain time-average density, velocity, and temperature measurements. In some cases, we attempted to obtain turbulence intensity measurements. Figure 6 shows a schematic of the experiment setup. The top section of the figure shows the setup around the jet facility including the laser, collection optics, and optical fiber. The lower section of the figure shows the optical processing system, which was located in a separate, quiet area away from the noisy jet since the processing equipment is extremely sensitive to vibration and temperature fluctuations.

A convergent nozzle was operated over a Mach number range of 0.15-0.95 in the subsonic flow regime, and at Mach 1.19 and 1.4 in the underexpanded flow regime. Since the measurement technique relies on having a clean gas flow, the unheated compressed air supplied to the primary jet was passed through micron filters to reduce the amount of dust, oil and water in the air. Additionally, an air blower and filter system provided a 200-mm diameter filtered, low speed (~20 m/s) coflow around the primary jet to clean the entrained ambient air. The coflow allowed particle-free measurements to be made well outside the shear layer and further downstream than would be possible otherwise. The total pressure of the air flow was measured by a pressure transducer located in the plenum of the jet.

A 5W, 532 nm, single-frequency, Nd:Vanadate CW laser with 2.25-mm output beam diameter provided the incident light for the system. The laser light was focused by a 350-mm focal length lens to a 200 μm diameter beam at the probe volume location. Rayleigh scattered light is polarization dependent, so a half-wave plate was used to align the peak scattering plane with the collection optics. The beam was oriented in the horizontal direction, 45° to the flow axis. The collection optics were arranged such that light was collected at a nominal scattering angle of 90°, and was first collimated by a f/3.67 300-mm focal length achromat, and then focused by a 160-mm focal length achromat on the face of a 0.55-mm diameter multimode optical fiber. The combination of fiber diameter, laser beam diameter, and magnification ratio provided a probe volume with a length of 1.03-mm and cross-sectional area of 0.155-mm^2.

The laser, transmitting optics, and receiving optics were all mounted on a x-y traversing system so that the probe volume could be moved to any location in the jet plume. The incident and scattering wave vectors were arranged such that the axial component of the velocity was measured. When necessary, a mirror and diffuser were placed in the beam path to direct unscattered laser light into the fiber for stabilization of the Fabry-Perot interferometer, and also to obtain reference laser fringe data.

The 20-m length optical fiber was routed to a separate room where the Fabry-Perot interferometer and detection optics were located. The lower section of figure 6 shows the layout of the detection system. The light exiting the fiber was collimated by an 80-mm focal length lens. A portion (~10%) of this light was split off and sent toward a set of photomultiplier tubes (PMT's) operated in the photon counting mode for the density measurement. The light that was split off was split again by a 50/50 beamsplitter before reaching the PMT's. Half of the light was sent to one PMT and half was sent to the other. Each PMT made an independent measurement of the density at the same point in the flow, and the average of the two PMT signals provided the mean density measurement. The rest of the light that was not sent to the PMT's was directed through the planar mirror Fabry-Perot interferometer. The interferometer had 70-mm diameter mirrors with 85% reflectivity, 9.6 GHz free spectral range (FSR), and reflective finesse of approximately 19.

When not acquiring flow data, a stabilization routine was performed to maintain parallelism between the Fabry-Perot mirrors and also to maintain a constant reference fringe radius. This procedure requires laser light to be directed into the optical fiber and through the Fabry-Perot interferometer, and a prism assembly to be placed at the output of the interferometer. The feedback data is collected by the video camera shown in the lower section of figure 6. Seasholtz et al[18] gives a detailed description of the stabilization procedure.

When obtaining flow data, the prisms were removed from the optical path and the light exiting the interferometer was focused by a 200-mm focal length fringe forming lens onto the detector of a slow scan, low noise CCD camera with 27-μm square pixels. This formed a 1.38 mm (50 pixel) diameter image of the fiber face at the detector plane. The diameter of the optical fiber limited us to imaging only the central fringe of the concentric fringe interference pattern.

A standardized procedure was used for collecting data at a single point in the flow field. The stabilization routine was used to maintain the reference fringe radius at the desired target value and the mirrors parallel during the times when spectral data was not being acquired. When the data acquisition cycle was started, the prisms that direct the fringes towards the stabilization camera were removed from the optical path and a reference fringe image was acquired using the low noise CCD camera and 10 ms exposure time. Figure 7a shows a typical fringe image formed by reference laser light obtained in this experiment. The mirror and diffuser, which allow reference laser light to be directed into the fiber in the test cell, were removed from the optical path so that the laser beam was directed through the probe volume in the flow field. Rayleigh scattered light from the probe volume was collected and sent through the optical fiber to the optical processing system. Two consecutive Rayleigh images were acquired using the CCD camera and 1 s exposure time. Figure 7b shows a typical fringe image formed by Rayleigh scattered light. The region of the detector where the measurements were taken happened to have some bad pixels. These pixels were not used in the image processing. The Rayleigh fringe shown corresponds to a velocity of 240 m/s. The peak of the Rayleigh fringe is shifted from the reference fringe peak by the Doppler shift associated with this velocity. For our experimental arrangement, the fringe diameter decreased as velocity increased. Also the Rayleigh fringe is more diffuse than the reference fringe due to thermal broadening.

Immediately following the capture of two Rayleigh fringe images, the PMT's were triggered to collect density data for 10 seconds at 10 kHz sampling rate. The mirror and diffuser were then replaced in the optical path to direct reference laser light to the optical processing location and obtain a second reference fringe image at 10 ms exposure time. The second reference fringe was used to check for drift in the laser frequency. If the fringe radius drifted by more than 3-μm between the first and second reference fringe images, then the Rayleigh data for that acquisition cycle was rejected. The prisms were moved back into the optical path and control was restored to the stabilization routine to reestablish the desired fringe radius, in case the system had drifted during data acquisition due to a change in laser frequency or temperature fluctuations inside the Fabry-Perot interferometer. The time needed to complete the acquisition process for a single data point was approximately 1 minute. This procedure was repeated for each data point.

RESULTS

Calibration

Reference fringe images were acquired over a range of fringe radii from 50 to 500 μm to determine an effective finesse relationship and incident intensity

pattern to use for the Rayleigh image processing. The reference images were fit for amplitude, A_f, effective finesse, N_e, fringe radius, r_R, and center position, (x_0, y_0). The baseline noise level was accounted for by subtracting a mean value at each pixel obtained from a series of images taken with the laser light off and the camera shutter closed. The finesse and intensity amplitude were functions of radius in the image plane as shown in figures 8 and 9. The reason that these parameters are not uniform across the image plane may be a result of defocusing as we move away from the lens centerline or imperfections in the Fabry-Perot mirrors. The finesse and intensity pattern relationships were incorporated into the model for the Rayleigh fringe analysis.

Calibration data for the Rayleigh scattered light was acquired over a range of velocities from 50 to 300 m/s (y = 0.7 to 0.9) to obtain an overall efficiency factor for the detection system. The calibration data were taken at a location in the flow that was 3 diameters downstream of the nozzle exit on the flow centerline where the true flow parameters are known relatively accurately from the isentropic flow equations. There was some question about the exact scattering angle of the optical system. Therefore, the Rayleigh image data were fit for scattering angle χ_s, effective efficiency ε, reference fringe radius r_R, and center position (x_0, y_0), while the density, ρ, velocity, u_k, and temperature, T, values were held fixed at the known isentropic values. Light at the laser frequency and light scattered from particles was negligible and was ignored in the model for analysis of all Rayleigh fringe data. The resulting scattering angle was approximately 92.3^o. Using this scattering angle in the model, the Rayleigh image data were fit for ε, r_R, x_0, and y_0, while the density, ρ, velocity, u_k, and temperature, T, values were held fixed to obtain a mean effective efficiency factor for each day that data was acquired. Turbulent velocity fluctuations σ_{u_k} were assumed to be zero since the probe volume was well within the potential core. The broadband light and read noise were accounted for in the same manner as in the reference fringe image processing described above.

The same calibration points that were used to determine the efficiency factor of the detection system were also used to calibrate the density data from the PMT's. A calibration was performed on each day that data was taken. The relationship between density and photon counts is linear, as shown in figure 10 where density is plotted as a function of mean photon counts for a typical calibration data set. The PMT data is used as a measure of the density rather than fitting for it in the least squares analysis since the density and temperature were partially correlated using the chosen model function.

The finesse and intensity profile relations were determined from data taken on one particular day and were applied to data taken on other days. Different effective efficiency factors were determined from the calibration data taken on each particular day and applied to data taken only on that day. For each day the efficiency factors were fairly repeatable with values being about 0.9%. The image files were fit for u_k, T, x_0, and y_0, with ρ determined from the PMT data. Figures 11, 12, and 13 show the differences between the measured density, velocity, and temperature and the isentropic values for four different run days with the calibrated finesse and intensity profile relations and efficiency factors applied. The reference fringe radius was obtained from the reference fringe image. Turbulence intensity was assumed to be 0% since previous analysis showed that measurements are not significantly affected by assuming zero turbulence for low turbulence cases. The standard deviation of the error is shown on each figure. The densities are within 1% of their true (isentropic) values, velocities fall within 2-3 m/s of their true values, and temperatures are within 2% of their true values. Although the finesse and intensity profile calibrations were not performed for each day of data collection, the accuracy of the recovered values on the other days was not sacrificed.

The calibration data was acquired at a location where turbulence levels were on the order of 1% or less ($\sigma_{u_k} \leq 3$ m/s). The images were analyzed again, this time also fitting for the turbulent velocity fluctuations rather than assuming them to be zero. The results indicate that the error in turbulence intensity was very high for these flows, and there is greater error as velocity decreases since the y-parameter decreases with decreasing velocity. Also, velocity fluctuations are very small at this location in the core of the jet, so we expect the turbulence estimates to have a high level of uncertainty. The temperature measurements also had higher errors than expected because the broadening of the spectrum was mistaken as broadening from turbulence. The high estimates of σ_{u_k} indicate that we cannot measure turbulence in these flows.

Converging nozzle, Mach 0.95 flow

An axial scan of Mach 0.95 flow issuing from a 25.4-mm diameter converging nozzle was performed along the jet axis. Pitot tube velocity data is available for similar flow conditions to use for comparison purposes. Figure 14 demonstrates good agreement between the velocities obtained using both measurement methods. This gives confidence that the

velocity results obtained from the Rayleigh scattering measurement method are reliable.

Underexpanded flows

Centerline axial scans were performed in Mach 1.19 and Mach 1.4 underexpanded flows using a converging nozzle. The Rayleigh image data were processed with the assumption that *TI* is zero, which is not exactly accurate, so the temperature calculations may be shifted from their true values since the additional broadening from turbulence may be construed as thermal broadening. Figures 15, 16, and 17 show density, velocity, and temperature as a function of axial position for Mach 1.19 and Mach 1.4 underexpanded flows. The isentropic flow conditions for fully expanded flow corresponding to the measured total and static pressures are shown on each plot as a reference, although the isentropic flow relations are no longer valid in these underexpanded flows. The shock structure can be seen in these plots as characterized by high to low velocity fluctuations. Figure 18 is a schlieren photograph of the Mach 1.19 underexpanded flow showing the shock structure. The temperature and density plots show fluctuations in accordance with the shock locations indicated by sharp velocity fluctuations in figure 16. The shocks in the Mach 1.19 flow are closer together than in the Mach 1.4 flow. Far downstream of the nozzle exit, the shock structure dissipates and the density approaches ambient. It is difficult to make a statement of accuracy for the velocity and temperature measurements since we do not have data to compare them with.

Discussion and Future Work

The density, velocity, and temperature measurements using the Rayleigh scattering technique described showed good agreement with expected values, even when turbulence is ignored. Extracting turbulence intensity proved to be a difficult task in the flows studied here. The ability to extract turbulence information is dependent on the shape of the Rayleigh spectrum. For y less than 0.8 the Rayleigh spectrum is close to Gaussian and the turbulence broadening, which is assumed to be Gaussian, cannot be separated from the Rayleigh spectrum. When y is greater than 0.8 the Rayleigh spectrum deviates from a Gaussian and allows the turbulence to be decoupled from the thermal broadening of the Rayleigh spectrum. Also, the uncertainty in turbulence is much greater for small values of σ_{uk}. From a lower bound uncertainty analysis we determined that the ability to obtain turbulence is restricted to flows were y is greater than 0.8 and σ_{uk} is greater than 10 m/s.

In the potential core of the jet flow, σ_{uk} is low and we cannot fit for turbulence. In regions outside of the mixing layer where temperatures are high, the y value is too low to extract turbulence. For our measurements, the only regions where we can expect to extract turbulence is in the mixing regions of high Mach number flows where temperature is low and the expected σ_{uk} is high. In general, we should be able to measure turbulence in cases where y is greater than or equal to 1. This is the case for high density flows at any scattering angle, and lower density flows using forward scattering. Although turbulence cannot be extracted in all cases, it has been shown that low levels of turbulence do not affect the ability to measure temperature, if we assume zero turbulence.

Based on the findings from this work there are several things we would like to look at in the future. We would like to make measurements in higher density flows and in low density flows using forward scattering to show that we can measure turbulence in these cases. In the current work, temperature fluctuations and aperture broadening were not taken into account in the model. A quick check indicated that aperture broadening would not significantly affect results of this study. Since extracting turbulence information is highly dependent on the shape of the spectrum, having the correct model for the spectrum is important. Both aperture broadening and temperature fluctuations will have an effect on the spectral shape and it is important to include their effects in the model.

There are several other approaches to measuring turbulence based on Rayleigh scattering. One approach is to record a number of instantaneous spectra using a pulsed laser and use the velocities obtained from these spectra to calculate the turbulence intensity. Another approach is to use the dynamic technique using a CW laser and high sampling rate data acquisition which we have developed independently of this work[18]. This technique works well for measuring velocity and density fluctuations, but currently is not capable of dynamic temperature measurement. A third approach is to add particles to the flow and use the spectral broadening of the peak resulting from particle scattering to measure turbulence. The width of the Mie scattering spectral peak is only the instrumental bandwidth of the Fabry-Perot when no turbulence is present. For turbulent flows, the broadening of the peak should give a sensitive measure of the turbulence.

CONCLUDING REMARKS

A Rayleigh scattering technique to measure time average velocity, density, temperature, and turbulence intensity was developed. The technique allowed measurement of density, velocity, and

temperature with accuracies of 1%, 2-3m/s, and 2%, respectively. Simulations showed that for low turbulence flows the estimates of density, velocity, and temperature are not significantly affected if turbulence intensity is assumed to be 0%. Comparison of pitot tube velocity data with velocity results from the Rayleigh scattering technique for Mach 0.95 flow showed very good agreement. Axial scans of two underexpanded flows revealed shock locations.

Turbulence intensity could not be recovered in any flow cases studied here due to either low turbulence or low y-parameter. Future work is planned to study higher y-parameter cases where it is expected that turbulence estimates can be made with some degree of accuracy.

REFERENCES

[1] Seasholtz, R.G., and Greer, L.C., "Rayleigh Scattering Diagnostic for Measurement of Temperature and Velocity in Harsh Environments," AIAA98-0206, 1998.

[2] Panda, J., and Seasholtz, R.G., "Velocity and temperature measurement in supersonic free jets using spectrally resolved Rayleigh scattering," AIAA99-0296, 1999.

[3] Lau, J.C., Morris, P.J., and Fisher, M.J., "Measurements in subsonic and supersonic free jets using a laser velocimeter," J Fluid Mech, vol. 93, pp. 1-27, 1979.

[4] Lau, J.C., Whiffen, M.C., Fisher, M.J., and Smith, D.M., "A note on turbulence measurements with a laser velocimeter," J Fluid Mech, vol. 102, pp. 353-366, 1981.

[5] Flack, R.D., "Influence of turbulence scale and structure on individual realization laser velocimeter biases," J Phys E: Sci Instrum, vol. 15, pp. 1038-1044, 1982.

[6] Heist, D.K., and Castro, I.P., "Point measurement of turbulence quantities in separated flows-a comparison of techniques," Meas Sci Technol, vol. 7, pp. 1444-1450, 1996.

[7] Elliott, G.S., and Boguszki, M., "Filtered Rayleigh Scattering: Toward Multiple Property Measurements," AIAA2001-0301, 2001.

[8] Li, Y., Roberts, W.L., and Brown, M.S., "Investigation of Gaseous Acoustic Damping Rates by Transient Grating Spectroscopy," AIAA Journal, vol. 40, pp. 1071-1077, 2002.

[9] Hart, R.C., Balla, R.J., and Herring, G.C., "Nonresonant referenced laser-induced acoustics thermometry in air," Applied Optics, vol. 38, pp. 577-584, 1999.

[10] Bridges, J., Wernet, M., and Brown, C., "Control of Jet Noise Through Mixing Enhancement," NASA/TM-2003-212335, 2003.

[11] Nakatani, N., Matsumoto, M., Ohmi, Y, and Yamada, T., "Turbulence measurement by the pulsed luminescence method using a nitrogen pulse laser," J Phys E: Sci Instrum, vol. 10, pp. 172-176, 1976.

[12] Garg, S., and Settles, G.S., "Measurements of a supersonic turbulent boundary layer by focusing schlieren deflectometry," Exp Fluids, vol. 25, pp. 254-264, 1998.

[13] Greytak, T.J., and Benedek, G.B., "Spectrum of Light Scattered from Thermal Fluctuations in Gases," Phys Rev Letters, vol. 17, pp. 179-182, 1966.

[14] Boley, C.D., Desai, R.C., and Tenti, G., "Kinetic Models and Brillouin Scattering in a Molecular Gas," Canadian Journal of Physics, vol. 50, pp. 2158-73, 1972.

[15] Tenti, G., Boley, C.D., and Desai, R.C., "On the Kinetic Model Description of Rayleigh-Brillouin Scattering from Molecular Gases," Canadian Journal of Physics, vol. 52, pp 285-290, 1974.

[16] Vaughan, J.M., *The Fabry Perot Interferometer, History, Theory, Practice, and Applications*, Adam Hilger, Bristol, pp. 89-134,1989.

[17] Whalen, A.D., *Detection of Signals in N*oise, Academic Press, New York, pp. 327-332, 1971.

[18] Seasholtz, R.G., Panda, J., and Elam, K.A., "Rayleigh scattering diagnostic for measurement of velocity and density fluctuation spectra," AIAA2002-0827, 2002.

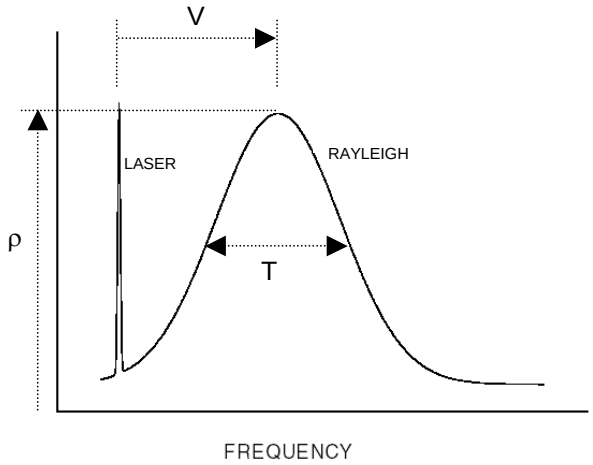

Figure 1. Rayleigh scattering spectrum.

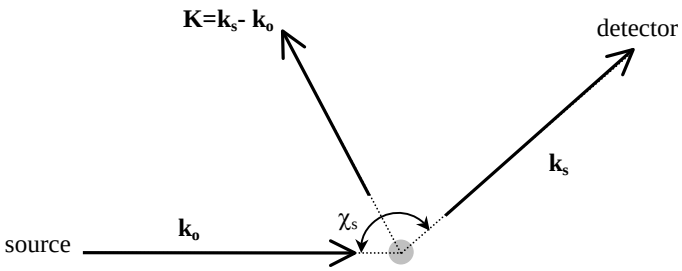

Figure 2. Light scattering from a moving particle.

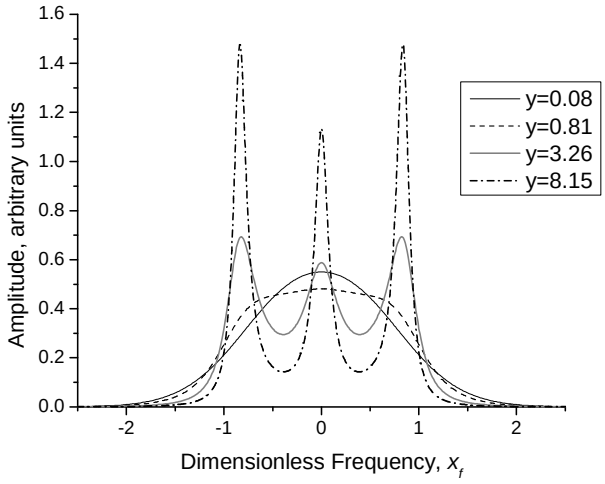

Figure 3. Rayleigh spectrum as a function of dimensionless frequency for various y-parameter values.

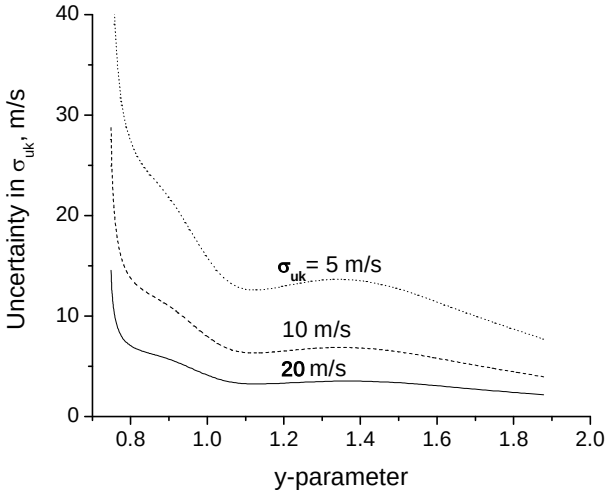

Figure 4. Lower bound for uncertainty in estimate of σ_{uk} as a function of *y*-parameter. Parameters fit are: ρ, u_k, T, σ_{uk}, x_0, y_0.

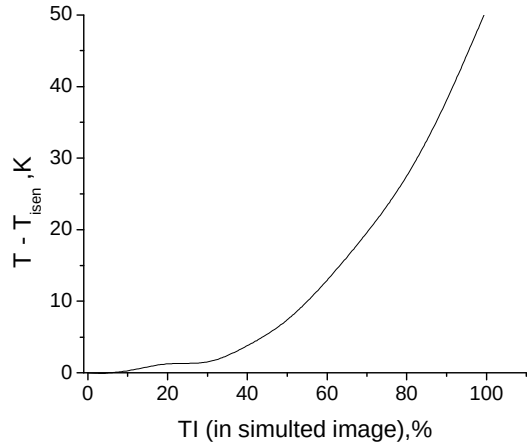

Figure 5. Error in estimate of temperature for Mach 0.6 flow. Turbulence is added to simulated image, but the fitting procedure assumes zero turbulence.

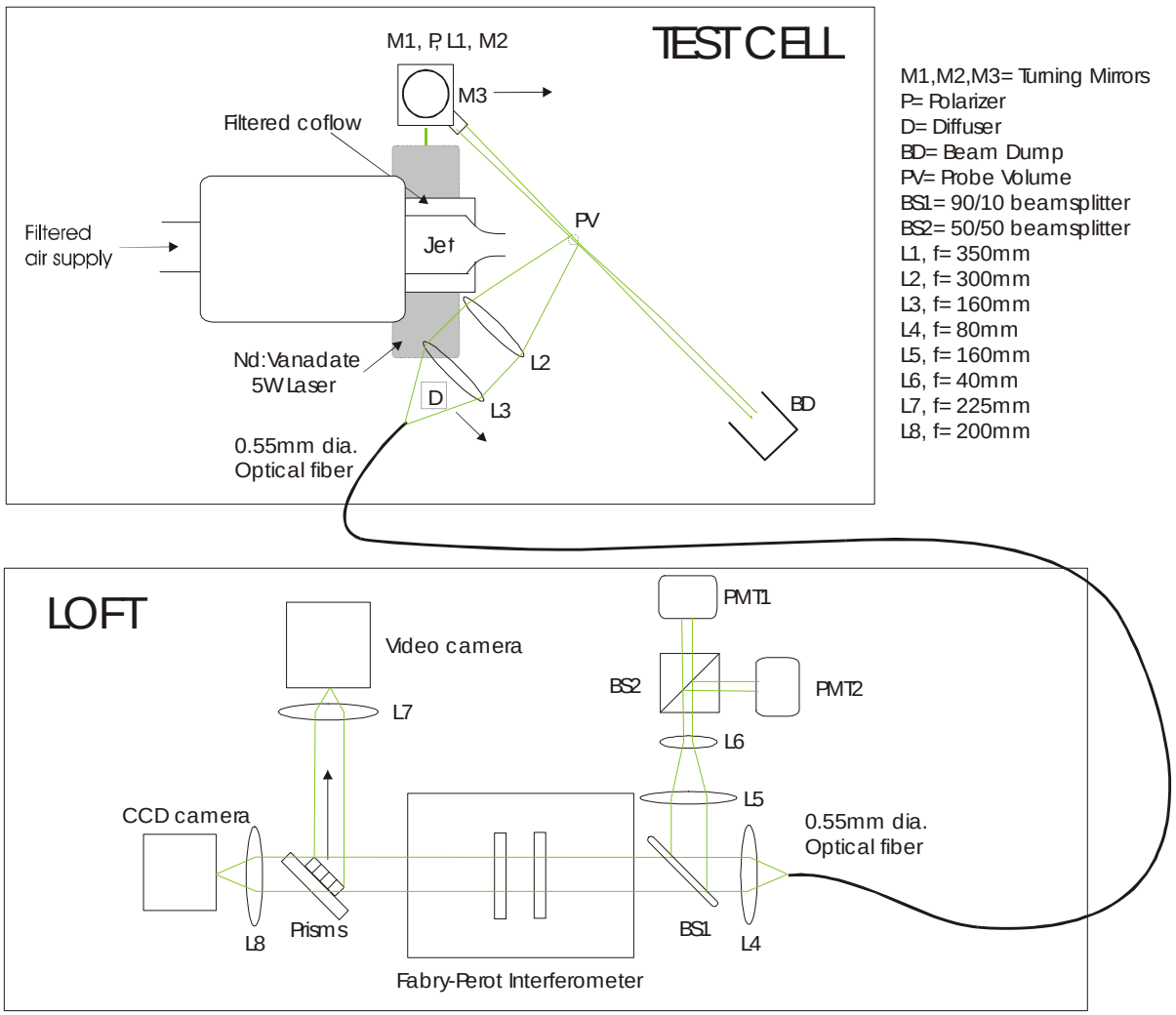

Figure 6. Schematic of experiment arrangement.

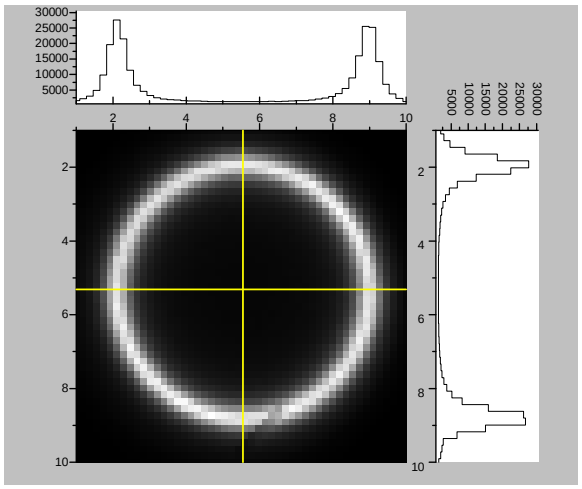

Figure 7a. Fabry-Perot fringe pattern image for the reference laser light.

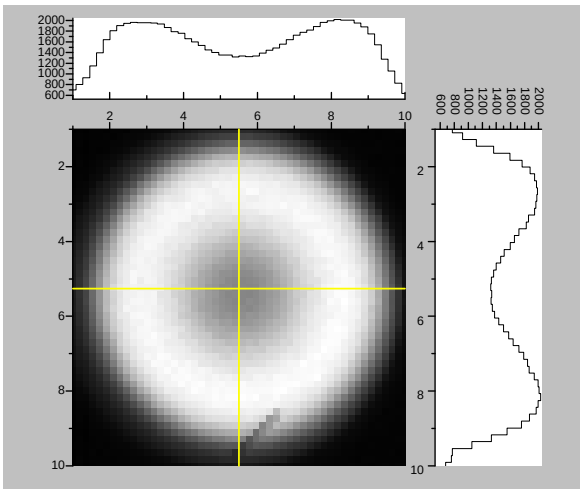

Figure 7b. Fabry-Perot fringe pattern image for Rayleigh light corresponding to a velocity of 240m/s.

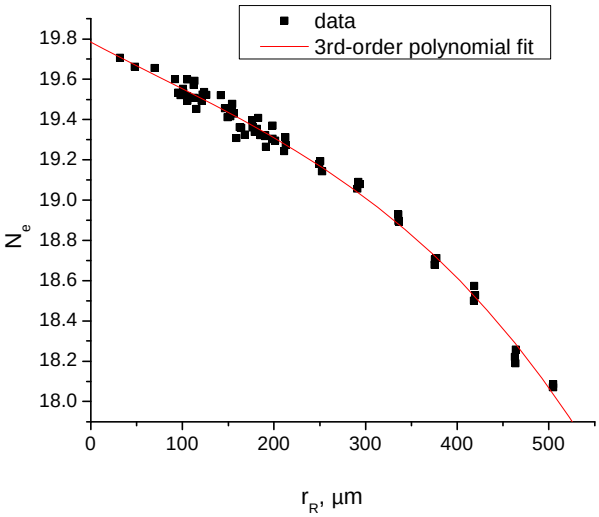

Figure 8. Effective Finesse as a function of radius using reference fringe images. Parameters fit are: A_f, Ne, r_R, x_0, y_0.

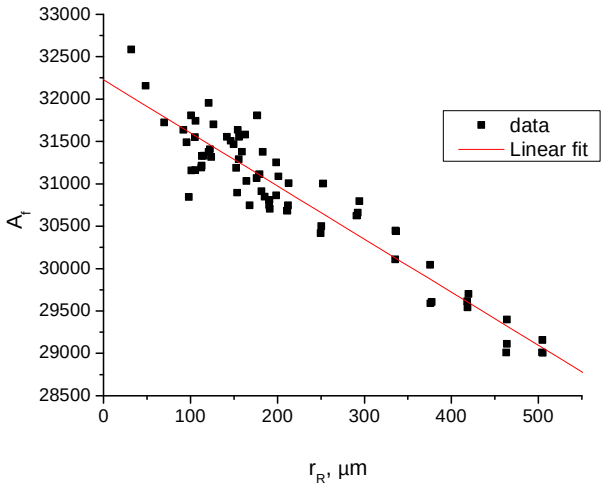

Figure 9. A_f as a function of radius using reference fringe images. Parameters fit are: A_f, Ne, r_R, x_0, y_0.

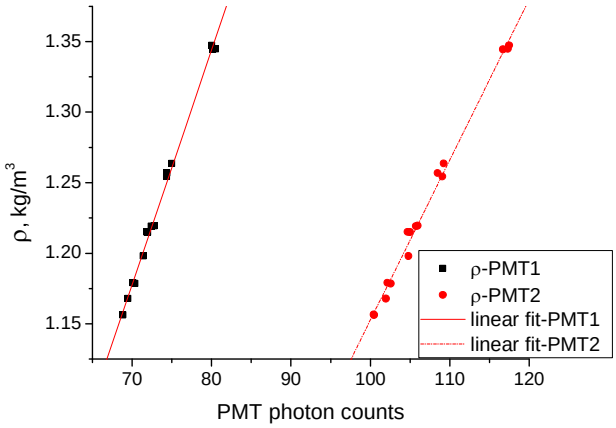

Figure 10. PMT calibration plot showing linear relationship between density and PMT photon counts.

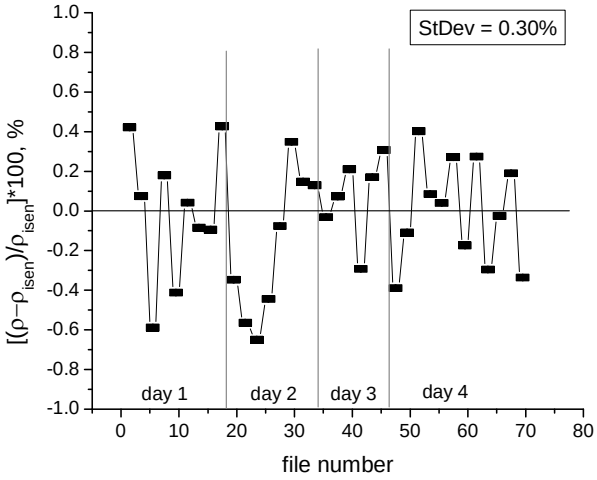

Figure 11. Relative error in density measured from PMT data for calibrations on four different run days.

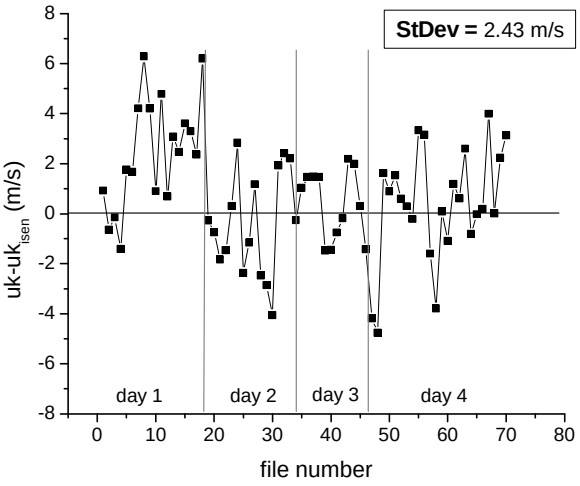

Figure 12. Velocity difference between measured and isentropic values for calibration data from four different run days. Parameters fit are: T, u_k, x_0, and y_0; TI=0%; ρ from PMT data. Isentropic velocities ranged from 50-300m/s.

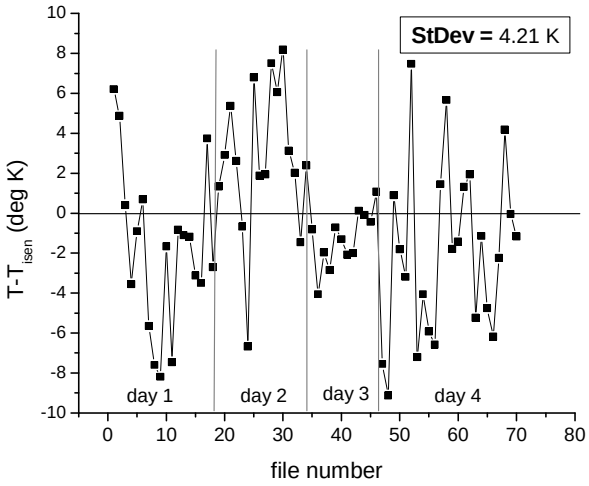

Figure 13. Temperature difference between measured and isentropic values for calibration data from four different run days. Parameters fit are: T, u_k, x_0, and y_0; TI=0%; ρ from PMT data. Isentropic temperatures ranged from 250-300 K.

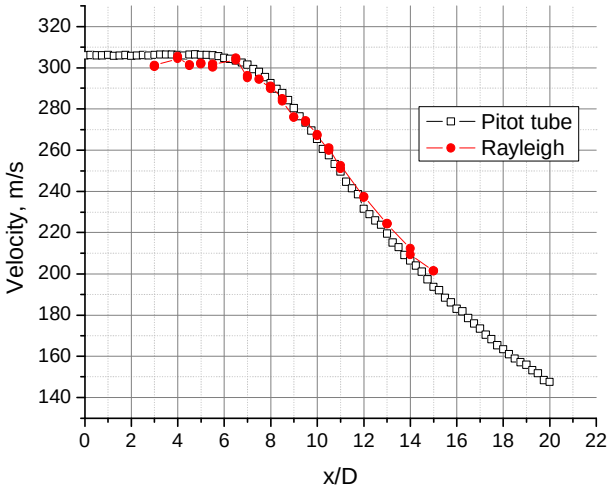

Figure 14. Pitot tube and Rayleigh velocity for Mach 0.95 axial centerline scan (axial distance normalized by nozzle diameter). Parameters fit are: T, u_k, x_0, and y_0; TI=0%; ρ from PMT data.

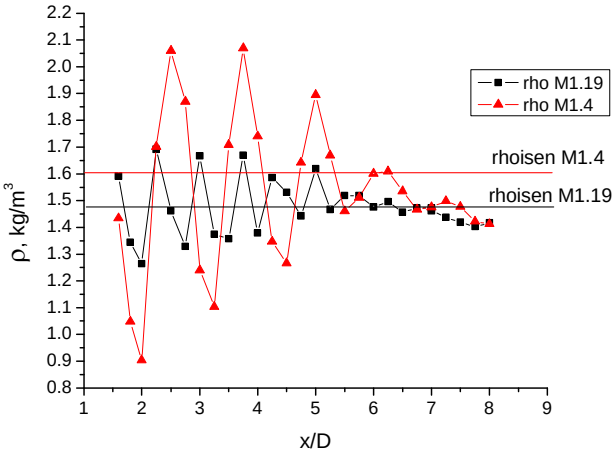

Figure 15. Density from PMT data for axial scans of Mach 1.19 and Mach 1.4 underexpanded flows. One measurement taken at each location.

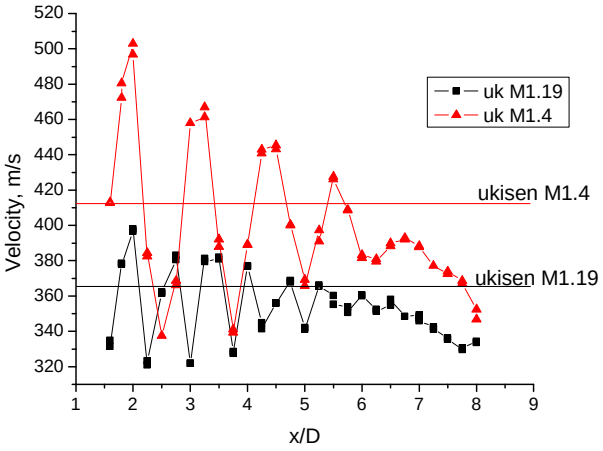

Figure 16. Velocity data for axial scan of Mach 1.19 and Mach 1.4 underexpanded flows. Parameters fit are: T, u_k, x_0, and y_0; TI=0%, ρ from PMT data. Isentropic velocity is shown as reference point for each Mach number case. Two measurements taken at each location.

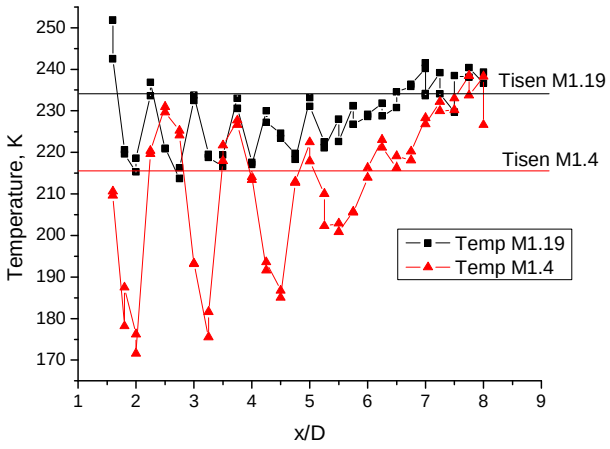

Figure 17. Temperature data for axial scan of Mach 1.19 and Mach 1.4 underexpanded flows. Parameters fit are: T, u_k, x_0, and y_0; TI=0%, ρ from PMT data. Isentropic temperature is shown as a reference point for each Mach number case. Two measurements taken at each location.

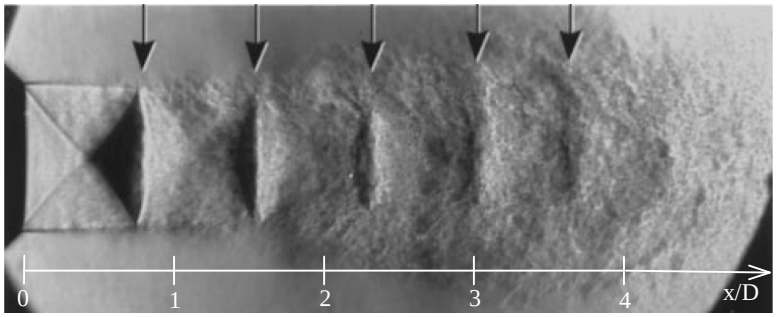

Figure 18. Schlieren photograph of the Mach 1.19 underexpanded jet. The shock locations are denoted by arrows.